PERGAMON

International Journal of Heat and Mass Transfer 42 (1999) 231–247

International Journal of HEAT and MASS TRANSFER

Heat transfer in a rotating two-pass smooth passage with a 180° rectangular turn

T.-M. Liou*, C. C. Chen

National Tsing Hua University, Department of Power Mechanical Engineering, Hsinchu 30043, Taiwan

Received 18 February 1997; in final form 7 April 1998

Abstract

Measurements are presented of the distributions of heat transfer coefficients along the leading and trailing walls of a rotating two-pass rectangular channel with through flow. The channel has a 180° rectangular turn and a cross-sectional aspect ratio of 1.25. The Reynolds number and rotational number were varied from 5.0×10^3 to 5.0×10^4 and 0 to 0.44, respectively. Complementary flow visualization and laser-Dopper velocimetry measurements were also performed to facilitate interpretation of the measured heat transfer distributions. The results show that the secondary flow induced by the curvature and turbulence enhancement associated with unsteadiness of separation bubble downstream of the sharp turn are responsible for the significant heat transfer augmentation attained in the first part of the second pass. Moreover, the quantitative effects of the Coriolis force on the skewness of streamwise mean velocity profiles and in turn different local and average heat transfer features in the radially outward and inward flows are demonstrated and addressed.

Nomenclature

A channel half-width [m]
A_p projected area of heating wall [m^2]
AR cross-sectional aspect ratio, A/B
B channel half-height [m]
C_p specific heat [J kg^{-1} K^{-1}]
d partitioner thickness [m]
D_H hydraulic diameter, $4AB/(A+B)$ [m]
h heat transfer coefficient [W m^{-2} K^{-1}]
k_f thermal conductivity of air at the film temperature [W m^{-1} K^{-1}]
k_w thermal conductivity of wall [W m^{-1} K^{-1}]
L actively heated length of each passage [m]
m mass flow rate [kg s^{-1}]
Nu local Nusselt number
Nu_0 Nusselt number in fully developed tube flow
Nu_S stationary local Nusselt number
$\overline{Nu}$ averaged Nusselt number
Pr Prandtl number of air, $\rho C_p v/k_{air}$
Q_{net} net heat transfer rate [W]
Q_{loss} heat loss rate [W]
q_{loss} heat loss per unit area [Wm^{-2}]
$\bar{R}$ mean rotation radius, $X_o+L/2$ [m]
Re Reynolds number, $U_b D_H/v$
Ra_Ω rotational Rayleigh number, $R\Omega^2\beta D_H^3 U_b(\Delta T)Pr/v^2$
Ro rotation number, $\Omega D_H/U_b$
rpm revolutions per minute [s^{-1}]
T_A ambient temperature [K]
T_b bulk mean temperature of air [K]
T_f film temperature $(T_b+T_w)/2$ [K]
T_w wall temperature [K]
ΔT wall-to-bulk temperature difference (T_w-T_b) [K]
U_b axial bulk mean velocity [m s^{-1}]
U axial mean velocity [m s^{-1}]
u axial turbulent intensity [m s^{-1}]
v transverse turbulent intensity [m s^{-1}]
X streamwise coordinate in the test section, Fig. 4
X_0 distance from rotating axis to the test-section minimum radius [m]
Y transverse coordinate, Fig. 4
Z spanwise coordinate, Fig. 4.

Greek symbols
ρ density of air [$kg\ m^{-3}$]

* Corresponding author. Tel: 00-886-3-5742607; Fax: 00-886-3-5749716; E-mail: tmliou@tmp.nthu.edu.tw

0017–9310/98 $19.00
PII: S0017–9310(98)00148–3

Ω rotating speed [s^{-1}]
ν kinematic viscosity [$m^2\ s^{-1}$]
ε eccentricity, $\bar{R}/D_H$.

1. Introduction

In advanced gas turbine engines the turbine inlet gas temperature (1700–2000 K) is much higher than the allowable temperature in blade metal alloys. Such high temperatures will shorten the creep life and accelerate material deterioration of the turbine blades or other components. Blade or vane cooling therefore becomes practical and critical. Many researchers have made efforts on the stationary channel cooling; however, the rotating effect on the heat transfer inside the serpentine cooling passages would be crucial in the thermal design of turbine blades. Both Coriolis force and buoyancy force result in secondary flows. These two secondary-flow driving forces can significantly alter the local heat transfer in the internal coolant passage.

Heat transfer data on turbine blade internal cooling under rotation are increasing yearly. Among the single-pass studies, Mori et al. [1] studied the mean convective heat transfer for laminar and turbulent flows in a rotating radial circular pipe by the use of a naphthalene-sublimation technique. Clifford et al. [2] reported the distributions of local and mean heat transfer coefficients for turbulent flow in a rotating triangular-sectioned radial duct based on thermocouple temperature measurements and pointed out the effects of sharp-entrance, sharp-exit and axial conduction of wall on the local heat transfer. Harasgama and Morris [3] presented the thermocouple measured heat transfer results of triangular, square and circular radial passages for turbulent flows. Different rotation effects on the leading- and trailing-wall heat transfer were reported. Morris and Ghavami-Nasr [4] studied heat transfer in a rotating rectangular duct with radially outward turbulent flow by the use of the thermocouple measurements. Enhancement of heat transfer on the trailing side was found, while impairment was found on the leading side. Soong et al. [5] experimentally studied a series of rotating rectangular radial ducts with different aspect ratios for Reynolds numbers in the range 700–20 000. The Coriolis effect was observed to be most significant for the ducts with aspect ratios near 1. Morris and Salemi [6] attempted to uncouple the effects of Coriolis and buoyancy forces on the turbulent flows in smooth circular tubes, rotating in an orthogonal mode, by using the thermocouple temperature measurements. A new parameter defined as the ratio of rotation number to buoyancy parameter was proposed to uncouple the effect of Coriolis forces from centripetal buoyancy. They found that buoyancy might either impair or improve local heat transfer on the leading wall depending on the values of the new parameter. Kuo and Hwang [7] conducted thermocouple temperature measurements similar to their previous study (Soong et al. [5]). Buoyancy was found to have opposite effects on the laminar and turbulent flows.

Most of the studies on heat transfer in multi-pass rotating channels are performed under turbulent flow conditions. Guidez [8] performed experimental and theoretical analyses for turbulent flows in a two-pass rectangular duct with a curved turn. His rotational rig was designed such that the curvature axis of the duct was parallel to the axis of rotation. Both thermocouple and infrared pyrometer techniques were adopted for experimental works. The numerical approach consists of a mixing length turbulence model and a major assumption of boundary-layer-type flow. Because of experimental difficulty, only results of the centrifugal channel (first pass) were presented. The measured results showed that duct rotation resulted in heat transfer augmentation on the trailing surface and deterioration slightly on the leading wall of the first pass. His numerical analysis revealed two opposite Coriolis-induced vortices in flow pattern calculations but did not include heat transfer predictions. Wagner et al. [9–10] experimentally studied turbulent heat transfer in a four-pass serpentine square-sectioned channel with smooth walls by the use of the thermocouple measurements. Large changes in heat transfer were found for radially outward flows due to variations of density ratio and rotation number, while relative small changes were found for radially inward flow. Yang et al. [11] performed thermocouple temperature measurements for turbulent flows in a four-pass serpentine square channel at low rotational speeds. Duct rotation was found to have a great effect on the value of local Nusselt number but little effect on circumferentially averaged values. Buoyancy effect was most prominent near the entrance but diminished along the flow passage. Significant heat transfer augmentation was found to occur near the sharp turns, which might be due to the presence of a strong secondary flow, although they did not provide experimental evidence to support this argument. Han and Zhang [12] and Han et al. [13] experimentally studied uneven wall temperature effect on local heat transfer for turbulent flows in a rotating two-pass square channel with smooth wall by the use of the thermocouple measurements. The uneven wall temperature was found to enhance local heat transfer and the effect was greater in the second pass.

It is obvious that more data are needed for a better understanding of the heat transfer characteristics in a rotating two-pass coolant channel, especially in the second pass. The aim of this study is to investigate the rotating effect on the turbulent heat transfer in a two-pass rectangular channel with smooth wall for Reynolds numbers and rotation numbers ranging from 5000 to 50 000 and 0 to 0.44, respectively. These conditions cover the ranges of the most previous experimental studies on rotating smooth ducts and are typically encountered in

a turbine engine. Air was used as coolant. Boundary conditions were constant heat flux on the trailing and leading walls and adiabatic on two side walls, which is closer to the conditions encountered in the cooling channel of actual turbine blades, for large temperature gradient existing between the leading and side walls or between the trailing and side walls. Moreover, because very few previous works tried to explain the heat transfer results with complementary flow visualization or/and flow field measurements, in the present work flow visualization and laser-Doppler velocimetry (LDV) measurements are performed to aid in understanding the measured heat transfer characteristics.

2. Experimental apparatus

The test model was designed to simulate a two-pass internal cooling channel of turbine blades (Fig. 1). A schematic drawing of overall experimental setup is shown in Fig. 2. The experimental apparatus is comprised of five main segments: rotor rig, coolant flow system, test section with heating module, temperature measurement and data acquisition system, and LDV system.

2.1. Rotating facility

The rotor rig consists of a hollow shaft and a hollow rotor arm mounted perpendicularly on the shaft. A counter balance mass is fitted on the opposite side of the rotor arm to attain static mass balance. The rotor is driven by a 10 kW DC motor with a variable frequency controller via a pair of pulleys and a toothed belt. The gear ratio of the pulley is 20/30, and the motor rating speed is 3430 rpm. The maximum rotating speed in the experiment is 1000 rpm, which leads to a gravitational force ranging from 400 to 940 g within the test section. The chassis of the rotating system is made of cast iron, which provides large inertia to reduce the amplitude of vibration. Four anti-vibration pads are used as isolators to abate vibration transferring into ground.

2.2. Coolant flow system

As shown in Fig. 3, the plenum cylinder is a part of the hollow shaft and is separated into two parts by the divider between the two passages. Ambient air is drafted into one side of the plenum cylinder in the hollow shaft, then turned 90° sharply into the first radial passage in the rotor arm. An unheated length of 244 mm in front of the test section is functioned as the flow developing region.

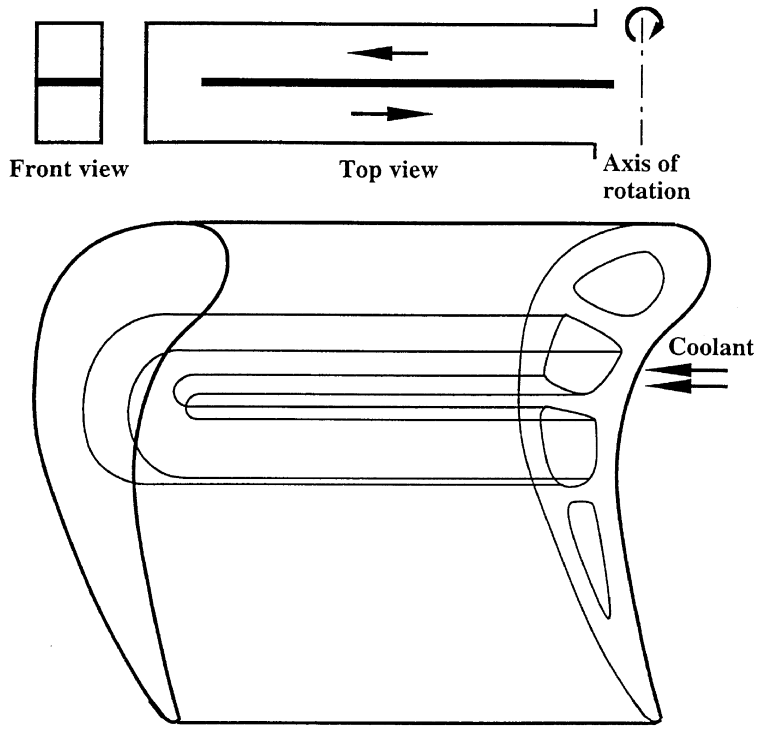

Fig. 1. Two-pass rectangular channel with smooth walls.

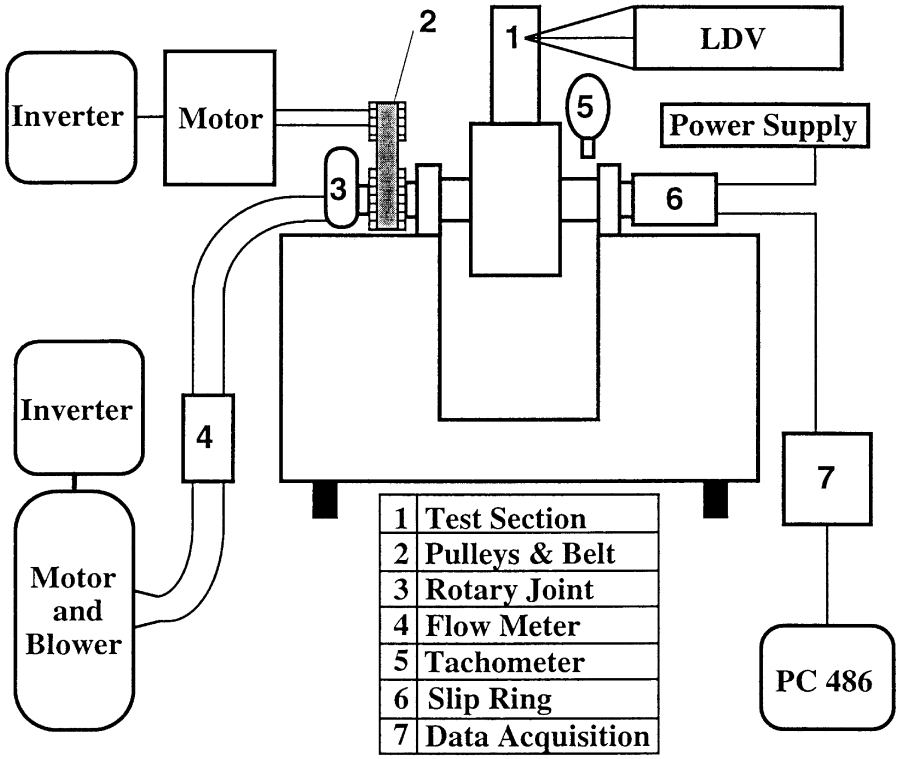

Fig. 2. The overall experimental setup for rotating internal cooling channel.

The effect of entry turning may still remain for such an unheated length; nevertheless, this is often encountered in a practical turbine blade's internal coolant passage. Air flows radially outward in the first passage and radially inward in the second passage after making a 180° sharp turn. The 'heated' air from the test section flows subsequently through the other side of the plenum cylinder in the hollow shaft, a rotary joint, a flexible pipe, a rotameter, and then is exhausted into ambient by a 2.2 kW turbo blower. The blowing flow rate can be adjusted by a frequency inverter controller. Several rotameters ranging from 100 to 2000 l min^{-1} are used to measure the coolant flow rate.

2.3. Test section

A two-pass rectangular duct has been assembled for this work to measure wall temperatures of the internal cooling channel flows in rotating and stationary modes. The configuration of the test model is shown in Fig. 4. Each passage of the test duct is 534 mm long. An unheated entrance region in first of the first pass is 244 mm long. The heated test section in the first passage is 270 mm long (L) and abutted by a 180° sharp turn. The heated section of the second passage is also 270 mm in length. Downstream of the second passage, there exists an unheated exit section of 244 mm in length. The flow passage has a rectangular cross-section of 20×16 mm^2 ($2A \times 2B$), given an aspect ratio of $AR = 1.25$ and a hydraulic diameter of $D_H = 18$ mm. $AR = 1.25$ was chosen since the previous single-pass study by Soong et al. [5] indicated the most significant effect of the Coriolis force on the turbulent heat transfer in the rotating ducts with a value of AR near 1. The mean rotating radius ($\bar{R}$) of the test section is 436 mm with an eccentricity (ε) of 24.2. The top and bottom walls of the passages are composed of aluminum plates heated by thermofoils. The leading and trailing walls are divided into 18 sections. Each section is constructed of two 0.8 mm-thick heated aluminum plates which are 27 mm in length and 18 mm in width. Silicon gel is filled along the periphery contact surface between aluminum parts to minimize longitudinal heat conduction. Thermofoils made of 0.005 mm-thick stainless-steel sheet are glued uniformly and flatly between the aluminum plates and the 10 mm-thick fiberglass boards by silicon adhesive. A 0.5 mm-thick

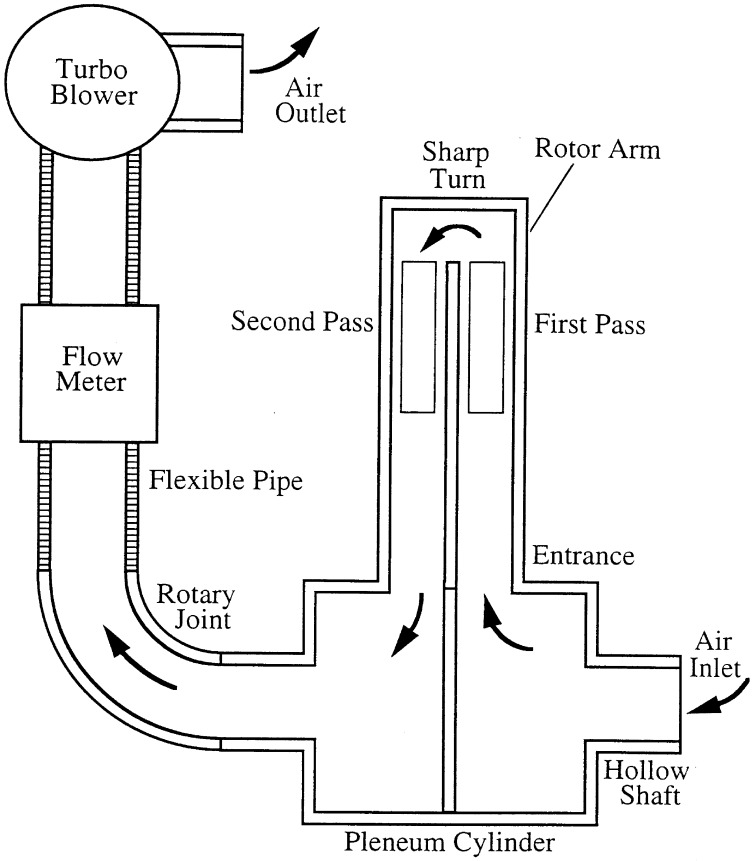

Fig. 3. Coolant flow system.

Teflon tape is placed between aluminum plates and the stainless thermofoils as an insulation of electricity. The back sides of thermofoils are insulated by fiberglass boards to prevent heat loss. The side walls are unheated and made of 5 mm-thick acrylic to provide optical access. The divider between the first and second passages is also made of 5 mm-thick acrylic. The thermofoils can be controlled by a 60 W DC power supply to provide constant heat flux at different power levels. The thermal resistance associated with the adhesive (about 0.1 mm) used at each interface is negligible (less than 2%).

2.4. Thermocouple and acquisition system

The first step in this work is to examine the wall temperature distribution in a smooth duct under the rotating condition by thermocouple measurements. The wall temperatures of the test section are measured by 36 copper–constantan thermocouples (i.e. T type) distributed along the leading and trailing walls (Fig. 4). The Teflon insulated fine gage single thermocouple has a wire diameter of 0.076 mm (0.003 in.). The junction-bead of the thermocouple is about 0.2 mm in diameter and is embedded into the center points of the grooves of the aluminum-plate surfaces. The inlet and outlet bulk mean temperatures are also measured by thermocouples. The measured temperature signals are transferred via a 36-channel slip ring to a data acquisition card (ADCLONE, ACL-812PG) and a PC-486 for data storage and further processing. The pre-processing of the raw data could be carried out by the use of a built-in program to calculate the non-dimensional parameters.

2.5. LDV setup

Figure 5 depicts the LDV experimental setup, which is similar to that described in Liou et al. [14], except for the phase angle identification. A two-color four-beam two-component LDV system was adopted. A 4-W argon-ion laser emitted the coherent light sources with 488 nm (blue) and 514.5 nm (green) lines. The forward scattering

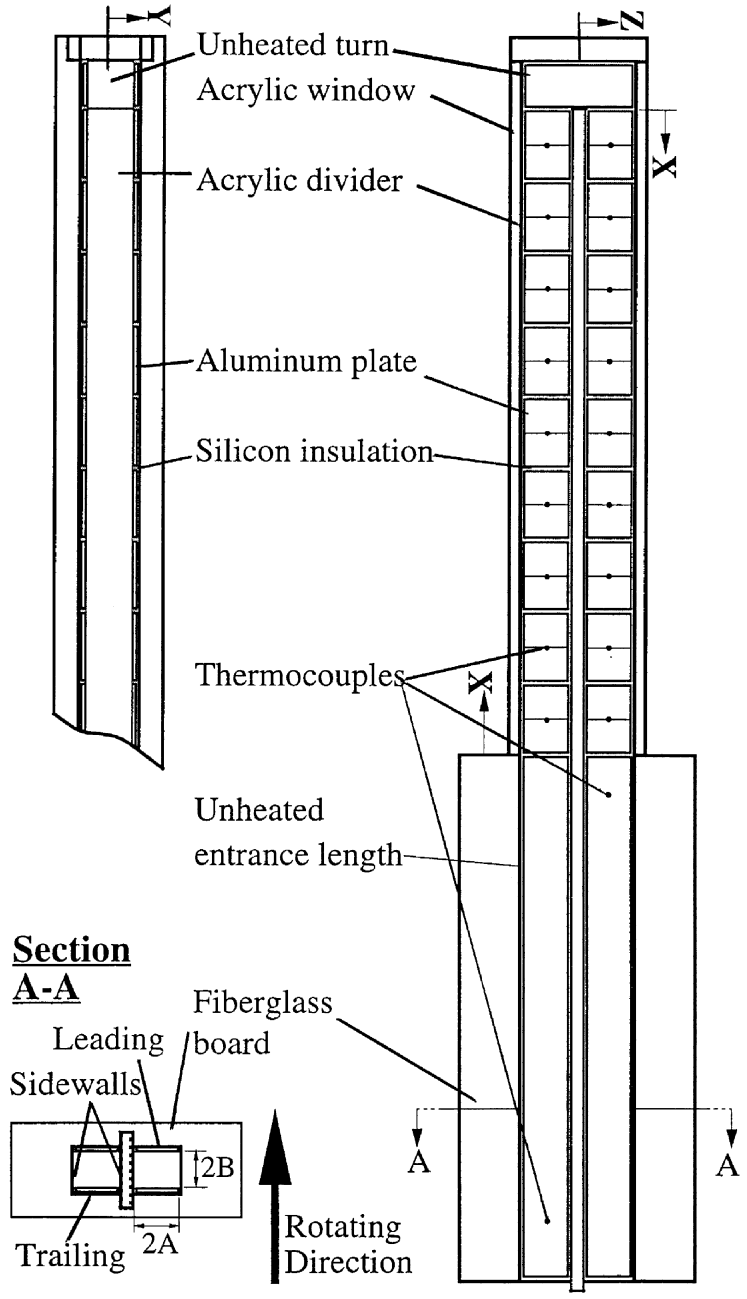

Fig. 4. Sketch of configuration and coordinate system of the test section.

configuration provided a probe volume of about 1.69 mm in length and 0.164 mm in diameter and the off-axis 0.74 mm in length and 0.164 mm in diameter inside the test section, based on e^{-2} extent of light intensity. The LDV system was mounted on a milling machine with four vibration-isolation mounts, allowing 0.01 mm positioning resolution of the probe volume. The light scattered from salt particles with a nominal 0.8 μm size was collected into the photomultiplier and downmixed to the appropriate frequency shift of 1–10 MHz. A phase angle processor was used to generate a trigger pulse at any selectable phase angle. The positioning window of each measuring location was indexed by the rotary encoder with a resolution (ER) of 0.125°. When a velocity measurement was validated by the counter processor, the phase angle-velocity data was transferred to the PC-586

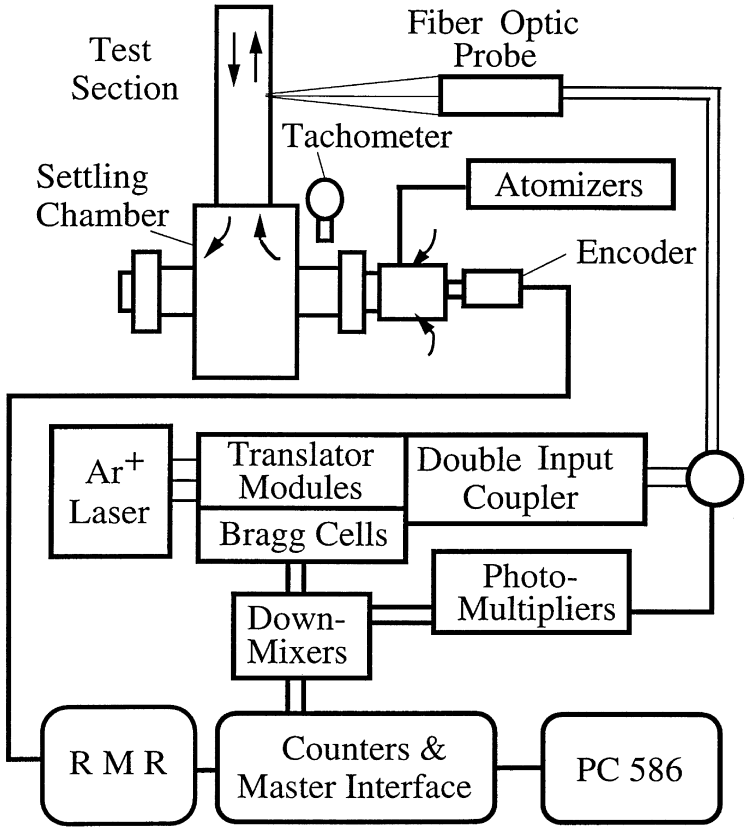

Fig. 5. LDV measurement system.

and recorded in separate data bins. Two circumferential traverses were performed along two close radial positions to obtain profiles along straight traverse lines by data interpolation.

2.6. Flow visualization system

The laser-sheet flow visualization used a 300 mW argon-ion laser as the light source and the smoke generated by burning Chinese incense sticks as the tracer particles. The smoke was sucked into the test section through the air inlet. When the examined area was illuminated by the light sheet, a JVC DV1 digital video camera was used to record continuous flow patterns. Pictures of selected instants were captured into a PC-586 for image-processing to attain clear images.

3. Data reduction

3.1. Governing parameters

For the gravitational force is negligible in comparison to the large inertia force and centripetal force, the heat transfer characteristics are governed by the inlet Reynolds number (Re), rotation number (Ro), buoyancy parameter (Ra_Ω), Prandtl number (Pr) and geometric factors [8]. Wagner et al. [10] showed that due to the vector nature of the equations of motion, flow direction has also a significant effect on the coolant flow characteristics in the rotating duct. In the present work, Prandtl number (Pr) is considered to be a constant value of 0.72 for air. The aspect ratio, eccentricity, and other geometric parameters of the two-pass channel are fixed as is the model. The functional relationship of the local Nusselt number with the parameters mentioned above can then be reduced to the following form:

$$Nu/Nu_0 = f(Re, Ro, Ra_\Omega, \text{flow direction}, X/D_H, Y/D_H, Z/D_H) \quad (1)$$

where Nu_0 is obtained from the heat transfer correlation for fully developed turbulent flows in smooth circular tubes without rotation (Dittus–Boelter, 1930)

$$Nu_0 = 0.023 Re^{0.8} Pr^{0.4} \quad (2)$$

Notice that in general Y/D_H and Z/D_H should be included. In the present study and in most previous studies [4, 5, 10], however, X/D_H is the only position effect

examined. The mean Nusselt number for the leading and trailing walls of each passage is also investigated. The position effect is canceled by the length-averaging process

$$Nu_m/Nu_0 = f(Re, Ro, Ra_\Omega, \text{flow direction}) \quad (3)$$

3.2. Heat loss estimation

Before the investigation of heat transfer coefficient distribution along the walls of the internal cooling channel, heat loss through the insulation walls to the external ambient and streamwise heat conduction via rotor arm to the rig need to be estimated first so that the net heat flux to the coolant can be calculated. In this series of tests, with no coolant flowing through the channel, the internal channel is filled with insulation stuffs to eliminate internal heat transfer by convection. The heater is supplied by a constant electric power until the wall temperature reached the steady state. The steady-state wall temperatures are measured for several power levels over a range of rotating speeds to establish the relationship between wall-to-ambient temperature difference ($T_w - T_A$) and the heat loss flux on the leading ($X/D_H = 0.8$–14.2) and trailing walls ($X/D_H = 0.8$–14.2) (Fig. 6). Streamwise distribution of internal wall temperatures could generate streamwise conduction data by a polynomial curve fitting. However, in the present study the insulated and separated heating plates minimize the streamwise heat flux that could be neglected in comparison to the total heat loss.

3.3. Nusselt number estimation

The local Nusselt number is calculated from

$$Nu = hD_H/K_f \quad (4)$$

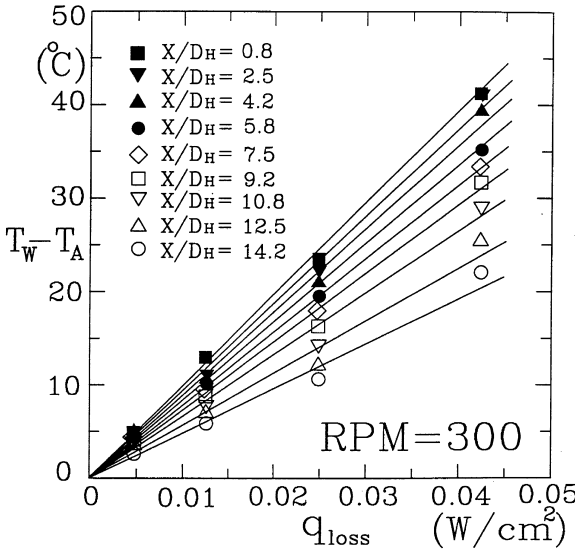

Fig. 6. The relationship between heat loss flux and wall-to-ambient temperature difference for rpm = 300.

where K_f is the air conductivity at the local film temperature. The film temperature, T_f, is defined as the average of the local wall temperature and bulk mean temperature

$$T_f = (T_w + T_b)/2 \quad (5)$$

The local heat transfer coefficient is calculated from net heat flux transferred into the coolant flow

$$h = Q_{net}/A_p(T_w - T_b) \quad (6)$$

where heat transfer area is always the projected area A_p of the heating walls, i.e. the smooth wall surface area. Net heat transfer is determined by subtracting the estimated heat loss from the heating power which is the product of heater voltage and current. The local wall temperatures (T_w) are measured values and the local bulk mean temperature (T_b) is determined by energy balance on each aluminum plate section. Coolant flow temperature will rise due to heat addition by the heating walls and its bulk mean value can be estimated as

$$T_b = T_0 + \Sigma Q_{net}/mC_p \quad (7)$$

where ΣQ_{net} is the total heat added to the coolant flow summated from the inlet of the test section to the local position X and m is the mass flow rate.

3.4. Uncertainty analysis

The method of single sample experiments proposed by Kline and McClintock [15] was applied to perform uncertainty analysis. By substituting equation (6) into equation (4), the Nusselt number can be further expressed as

$$Nu = Q_{net}D_H/K_fA_p(T_w - T_b) = (I \cdot V - Q_{loss})D_H/K_fA_p\Delta T = (mC_p\Delta T_b)D_H/K_fA_p\Delta T \quad (8)$$

where I is the heating current supplied to the heating foils, V the voltage supplied across the heater, Q_{loss} the heat loss, ΔT_b the difference between bulk inlet temperature and bulk outlet temperature, and m the air mass flow rate. The temperature uncertainty in the thermocouple and acquisition system is estimated to be ± 1°C. The value of $T_w - T_b$ varies from 8 to 40°C. The non-dimensional uncertainty intervals for the variables in equation (8) are listed as follows:

power inputs	$IV \pm 2.5\%$
air mass flow rate	$m \pm 5.0\%$
specific heat of air	$C_p \pm 0.5\%$
thermal conductivity of air	$K_f \pm 0.5\%$
hydraulic diameter	$D_H \pm 0.5\%$
heating area	$A_p \pm 1.0\%$
temperature	$T \pm 2.5$–12.5%

According to root-sum-square method, the most proper uncertainty is estimated to be less than 10% for Reynolds number larger than 10 000. The maximum uncertainty, 23%, occurs for the lowest heat transfer coefficient at the lowest Reynolds number ($Re = 5000$). The uncertainty of Nusselt number is a function of X/D_H and mainly

influenced by the wall-to-bulk temperature differences $\Delta T(x)$.

4. Experimental conditions

In the present study, four Reynolds numbers, $Re = 5000$, 10 000, 30 000, and 50 000, and five rotational speeds, $\Omega = 0$, 300, 500, 750 and 1000 rpm, were investigated. The corresponding rotational numbers thus ranged from 0 to 0.44. Only one heating condition was tested: leading and trailing walls at the same heat flux with sidewalls unheated and insulated. T_w was varied in the range 30–70°C. Hence, the rotational Rayleigh number was 0 and from 2.32×10^5 to 1.31×10^7. Flow direction in the two-pass radial channel was outward in the first pass and inward in the second pass. Notice that the X-coordinate origin was chosen at the entrance of each pass, as shown in Fig. 4. In each pass, heat transfer coefficients were examined at $X/D_H = 0.8$, 2.5, 4.2, 5.8, 7.5, 9.2, 10.8, 12.5 and 14.2. Complementary flow visualization at $Re = 2500$ and LDV measurements of the interesting region at $Re = 1.4\times10^4$ with $Ro = 0$ and 0.08 were also performed to facilitate the understanding of measured heat transfer characteristics.

5. Results and discussions

5.1. Stationary case

The first step of the study was to determine the Nusselt number distribution of the two-pass cooling channel without rotation. It serves as the reference case so that the effects of rotation may be determined by comparing the measured results with and without rotation. As shown in Fig. 7, the results at $Re = 5000$, 10 000 and 30 000 were compared with the Dittus–Boelter (1930) correlation values. The Nusselt number increases monotonically with increasing Reynolds number while the shape of the Nu_S vs X/D_H curve is preserved. In the first passage, the Nusselt number first decreases with increasing X/D_H indicating a developing flow in the thermal entrance region, subsequently approaches the fully developed value (equation (3)), and then increases slightly near the end of the first passage ($X/D_H = 12$) because of the upstream effect of the sharp turn. The present measured Nu distribution in the first passage agrees with the previously reported local heat transfer characteristics in the entry region of a circular tube [17]. The deviation of measured values from the Dittus–Boelter correlation believed is to be the results of different inlet flow conditions, thermal boundary conditions and the test section configurations. Also note, that because only one thermocouple was used to present a regional averaged temperature, the local difference of heat transfer within a region is ignored in our work. In fact, this deviation is also found in previous studies [2, 4, 10]

In the first part of the second passage ($X/D_H < 7$, Fig. 7), the heat transfer coefficients are enhanced greatly due to the 180° turn and a developing process followed. More specifically, according to the laser-sheet flow visualization results, when coolant flow passes through the sharp turn, curvature-generated secondary flow (90–180° in Fig. 8, view from downstream side) and turbulence enhancement resulting from sharp turning geometry induced flow separation (Fig. 9) significantly augment the heat transfer. It should be mentioned that there are lacking noticeable secondary flow structures at 0° and 45° cross-sections of the turn, as shown in Fig. 8, to enhance the heat transfer rate in the first part of the turn. The shifting of the core flow region toward the partition wall (i.e., inner wall) at 45° cross-section of the turn (Fig. 8) is due to the presence of the corner recirculating flow region depicted in Fig. 9 for the case of $Ro = 0$. The corner recirculation zone measures about $0.4\pm0.1D_H$ in length and $0.4\pm0.1D_H$ in height in the plane of symmetry $Y/B = 0$. In the second part of the turn, the well-known Dean vortices appear. The well-organized counterrotating vortex pairs at 90 and 135° cross-sections are more stable than the vortex pairs at 180° cross section or the entry of the second pass. The flow unsteadiness at the entry (i.e., 180° cross-section or near $X/D_H = 0.1$) of the second pass (Fig. 8) is associated with the occurrence of the unsteady large separating bubble immediately downstream of the turn, as shown in Fig. 9 for the case of $Ro = 0$, which has a length of 2.7 ± 0.3 D_H and a height of $0.6\pm0.07D_H$ in $Y/B = 0$ plane. In view of the flow visualization ($Re = 2.5\times10^3$) and heat transfer results ($Re = 5\times10^3$ to 5×10^4) were taken at different Reynolds numbers, a sensitivity check of the separation bubble size to the values of Re is necessary. A near-wall LDV scanning (the probe volume of LDV was placed 1 mm from the wall) at $Re = 1.4\times10^4$ was therefore performed. By graphing the velocity at each point, the position at which the axial mean velocity changes sign could be found. The reattachment length thus determined, as shown in the top of Fig. 9, was 2.0 D_H which is about 75% of that visualized at $Re = 2.5\times10^3$. This comparison is in good accord with the previous heat transfer results showing the reduction of the separated-flow low heat transfer zone with increasing Reynolds number, using a transient liquid crystal image technique [18].

Also, notice that there exists an additional counterrotating vortex pair near the inner wall at 180° cross-section of the second pass, as compared with the single counterrotating vortex pair at 90 and 135° cross-sections inside the turn (Fig. 8). The interaction of the two pairs of counterrotating vortex structures at 180° cross-section (or near $X/D_H = 0.1$) of the second pass, one pair located inside and the other outside the separating bubble, also contributes to the flow unsteadiness and in turn tur-

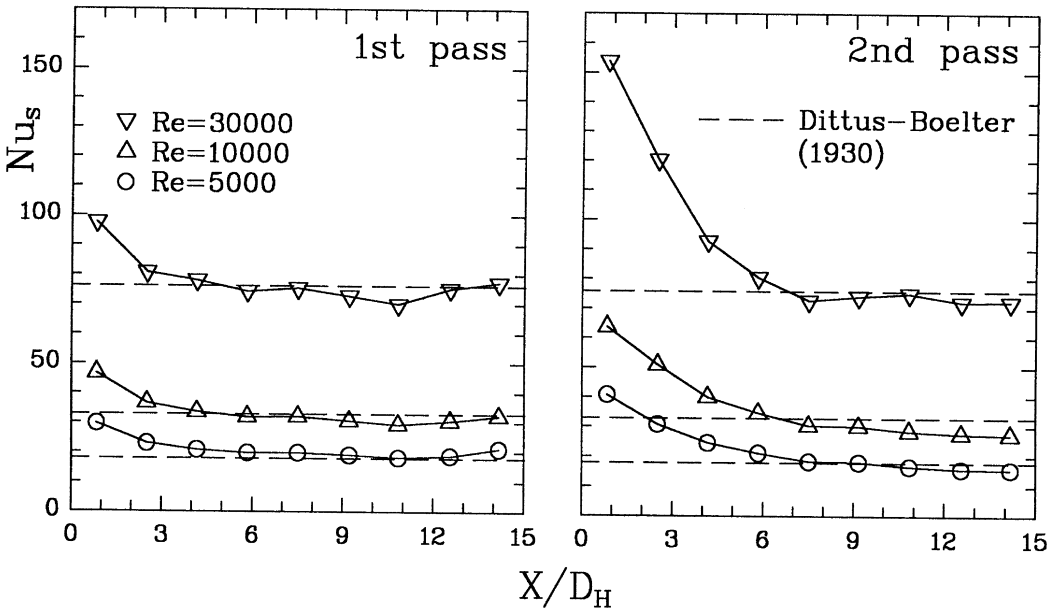

Fig. 7. Streamwise heat transfer coefficient distributions in the two-pass stationary duct at various values of *Re*.

bulence enhancement in the first region of the second pass. Quantitatively, the complementary LDV measurements around the sharp turn reveal the great enhancement of turbulence intensity, as demonstrated in Fig. 10. It is seen that the turbulent kinetic energy defined as $(\overline{u}^2+\overline{v}^2)/(2U_b^2)$ is increased from 1% before the turn to 24% in the separating bubble after the turn. At the end of the second passage, the Nusselt number approaches the correlation value of equation (3) again, as shown in Fig. 7. Note that the differences in Nusselt number between the leading and trailing walls are less than 5% for the range of Reynolds number examined. Hence, only one curve is used to present both distributions on leading and trailing walls.

5.2. Rotating case

Figure 11 shows the wall temperature distributions for the two-pass turbulent duct flow of $Re = 3\times10^4$ with ($Ro = 0.073$) and without ($Ro = 0$) duct rotation. In general, the temperature differences between the leading and trailing wall are larger in the first pass than in the second pass, which is due to the opposite directions of the Coriolis-induced secondary flow for the outward (first pass) and inward (second pass) flows, as will be illustrated shortly. In the first passage, the leading wall temperatures are higher for the rotating case (symbol ● than for the stationary case (symbol+), while the trend is reversed for the trailing wall temperatures (symbol ○). In the second passage, both leading and trailing wall temperatures are lower with rotation than without rotation. As a result of the above fact, the leading wall of the outward flow is susceptible to heat transfer deterioration.

Figure 11 also illustrates the effect of rotation on the local Nusselt number ratio distributions ($Ro = 0.055$). In the first passage, the trailing wall Nusselt number ratio level of the rotational case is higher than that of the stationary one while the trend is reversed for the leading wall Nusselt number ratio level. At this point, it is worth pointing out that the previous observations based on the single-pass studies [3, 4] are basically in agreement with our measured results for the first pass. However, our measured heat transfer results in the second pass are greatly different from the previously reported single-pass results.

In the second passage the Nusselt number ratio level of the stationary case is the lowest in most cases; moreover, the Nu/Nu_0 level of the leading wall is higher than that of the trailing one for the rotating case. Notice that the Nu/Nu_0 level of the leading wall is the lowest in the first pass, whereas it is highest in the second pass. The above different behaviors are attributed to the direction of the Coriolis-induced secondary flow, and can be realized by comparing our LDV measurements between $Ro = 0$ and 0.08, as depicted in Fig. 12. It is observed that in the radially outward flow, top of Fig. 12, the Coriolis force due to rotation ($Ro = 0.08$) shifts the symmetric streamwise mean velocity profile of $Ro = 0$ (curve with symbol □) toward the trailing wall (curve with symbol ■) while in the radially inward flow, bottom of Fig. 12, the Coriolis force shifts the streamwise main flow of $Ro = 0$ toward the leading wall. Note that the mean

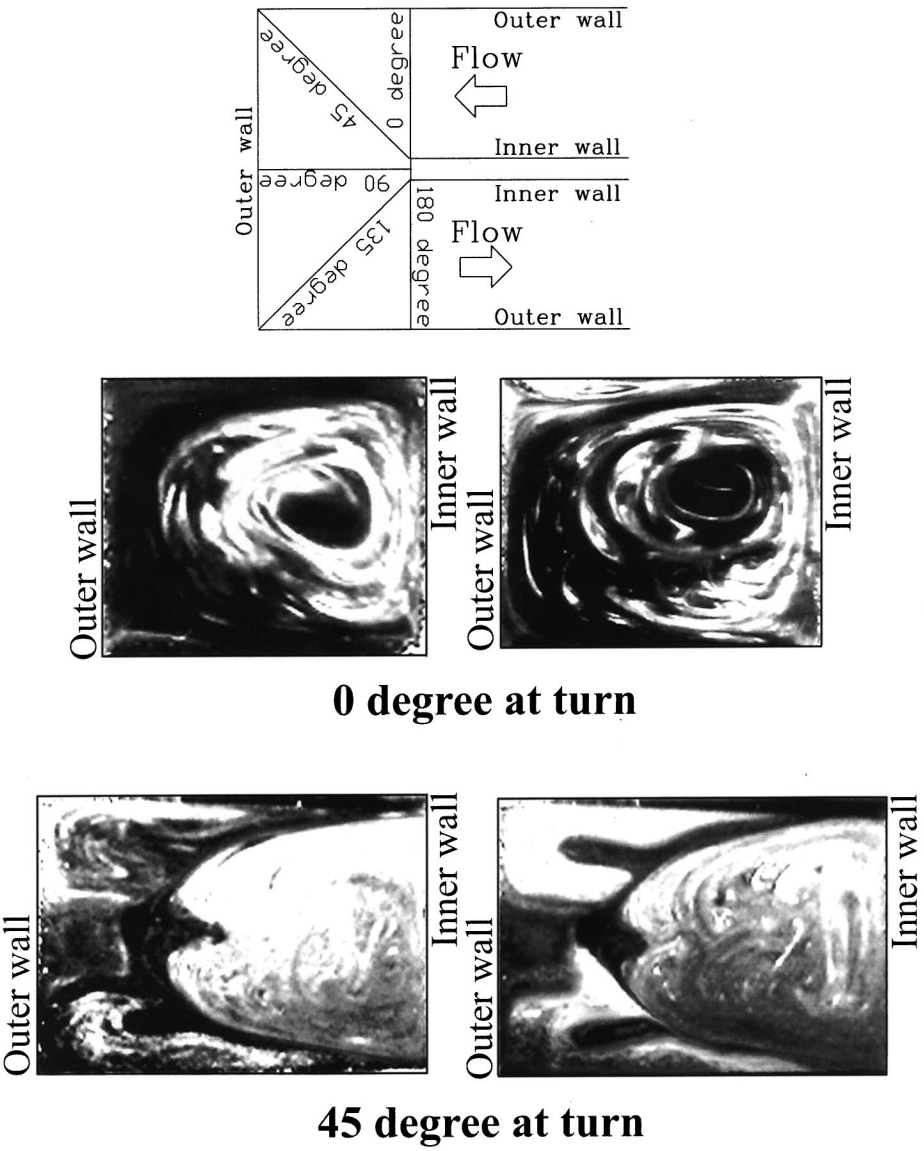

Fig. 8. Secondary flow patterns from two different instants at 0, 45, 90, 135 and 180° cross-sections of turn ($Ro = 0$ and $Re = 2500$). (View from downstream side.)

velocity in Fig. 12 is positive along the streamwise direction.

Figure 11 further shows that the differences of heat transfer coefficient ratio between the leading and trailing walls are larger in the first passage than in the second passage. A possible explanation is that the centrifugal buoyancy force enhances the Coriolis effect and, in turn, accelerates the cold core stream in the first passage, while in the second passage, because the flow direction is reversed, buoyancy force retards the cold core stream and thus countervails the Coriolis effect, as pointed by Han et al. [13] in studying the uneven wall temperature effect on the local heat transfer in a two-pass turbine blade cooling channel. Moreover, in the first part of the second pass, the heat transfer augmentation is mainly contributed by the turn induced secondary flow and the high turbulent intensity. Near the inner wall, a recirculation bubble exists with relatively low heat transfer rate. It is believed that in the first part of the second pass, the test section configuration has a stronger effect on the heat transfer characteristics than does the rotation. Further downstream, however, because the secondary-flow patterns of the turn-induced Dean-type vortices (Fig. 8) and the rotation-induced vortices are different—

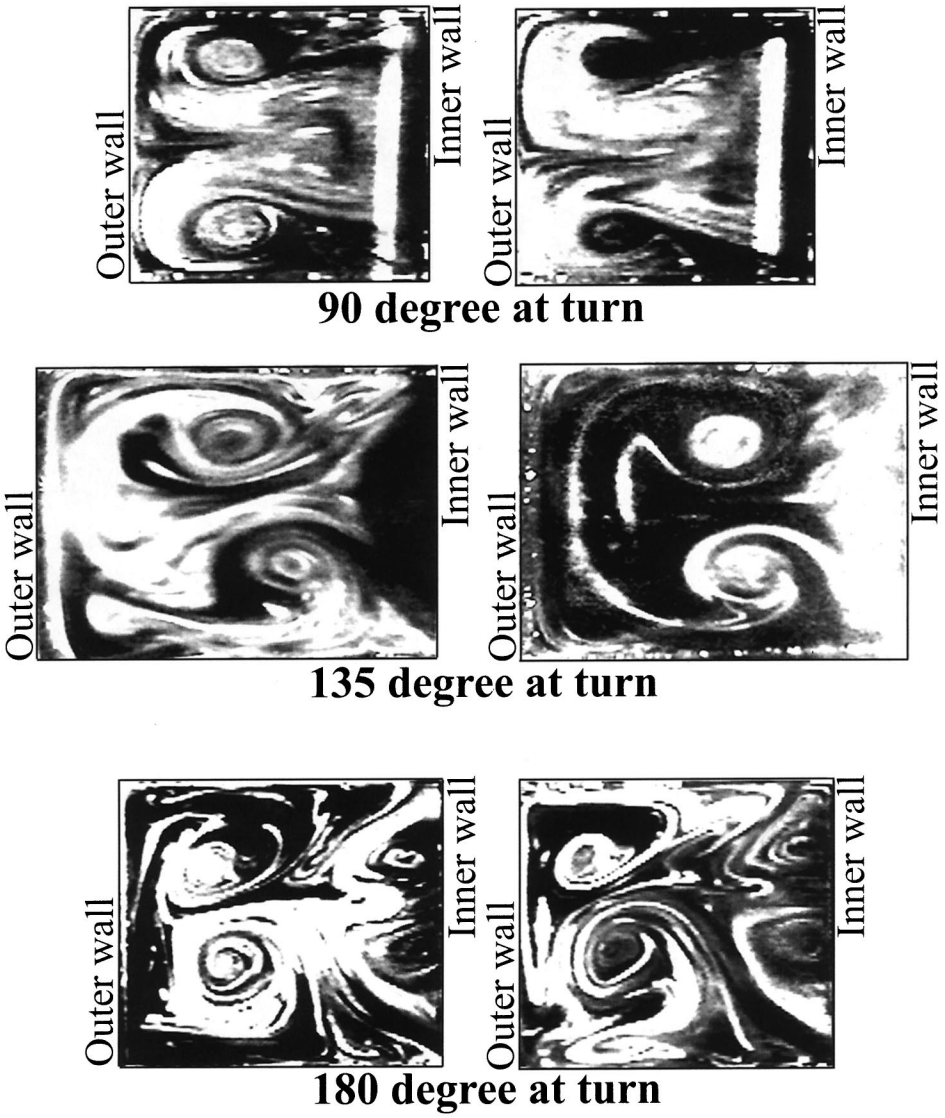

Fig. 8—*continued.*

the symmetry planes are horizontal (e.g., 180° in Fig. 8) and vertical for the former and latter cases, respectively—there will be a range of X/D_H within which the aforementioned two types of streamwise vortices interact each other to form another rather complex secondary flow pattern. Although, due to experimental difficulty, we have not yet gathered detailed flow and heat transfer data to support this point, it could be the reason for the least and larger differences in Nu/Nu_0 levels of the leading and trailing walls around $X/D_H = 0 \sim 4$ and downstream of $X/D_H = 5$, respectively, in the second pass for the rotating case. The slight increase of Nu/Nu_0 level from $X/D_H = 6$–9 reflects the characteristics of the test section, as can also be found from the previous result [4].

5.3. Rotation number and location effect

Figure 13 shows the length-averaged Nusselt number ratio vs rotation number for $Re = 5000$, 10 000, 30 000 and 50 000. Two observations can be made. First, the Nu/Nu_0 differences between the leading and trailing walls in both passages are found to increase with increasing rotation number. The rotation effect is more prominent in the first pass than in the second pass, a result similar

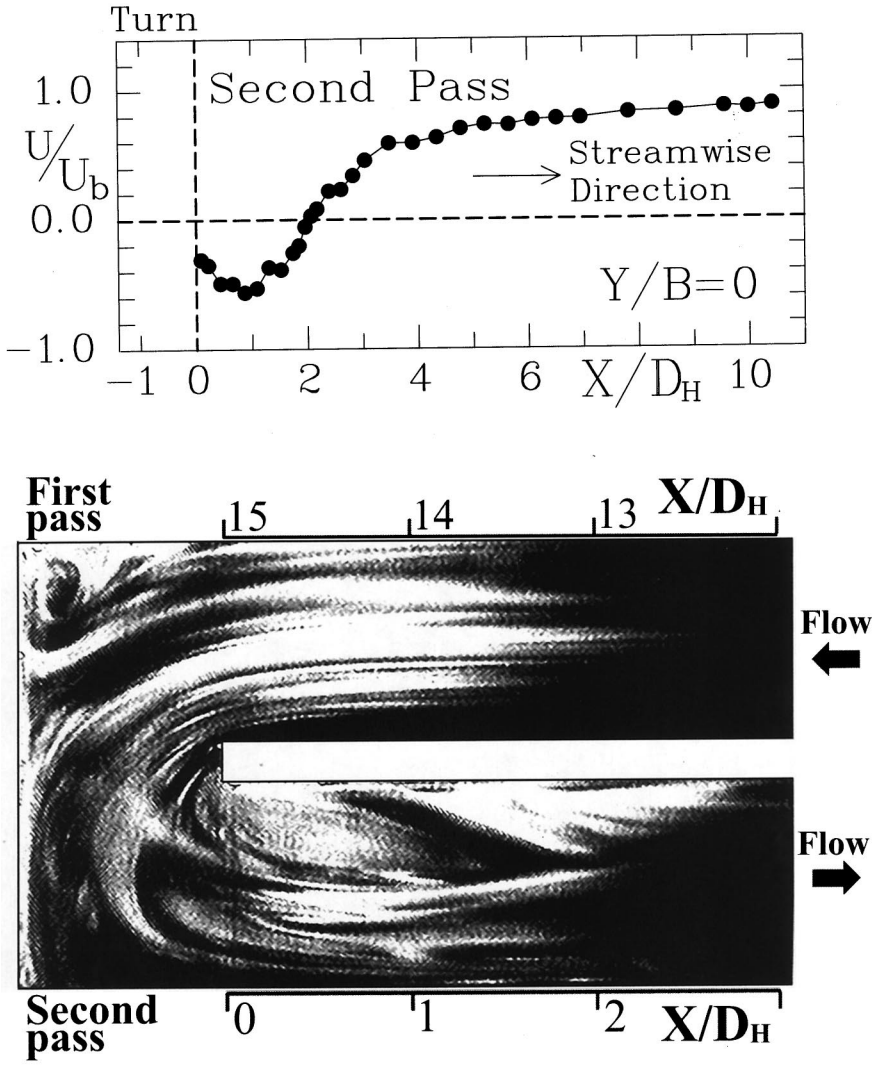

Fig. 9. Flow pattern in the streamwise plane $Y = 0$ ($Ro = 0$ and $Re = 2500$) and variation of streamwise mean velocity along a line 1 mm away from the divider wall for $Ro = 0$ and $Re = 14\,000$.

to that observed by Wagner et al. [10] in studying a four-pass rotating cooling channel. Second, the effect of Ro on the averaged heat transfer coefficient is quite different between the first and second pass. In the first pass, as Ro increases, $\overline{Nu}/Nu_0$ increases and decreases on the trailing and leading walls, respectively. As a result, for the highest rotational number examined, $Ro = 0.44$, the $\overline{Nu}/Nu_0$ of the trailing wall can be as high as three times that of the leading wall. In contrast, the values of $\overline{Nu}/Nu_0$ on the leading and trailing walls of the second pass increase with increasing Ro. The increasing rate of the former is slightly faster than that of the latter. As a result, the $\overline{Nu}/Nu_0$ difference between the leading and trailing walls of the second pass increases slowly; as $Ro = 0.44$ the $\overline{Nu}/Nu_0$ of the trailing wall is 1.4 times that of the leading wall.

The experimental results of Han et al. [13] for the case of four walls heated at the same temperature are also included in Fig. 13 for comparison. Note that the results of the Han et al. for $Ro = 0.035$–0.35 were obtained from $Re = 2.5\times10^3$ to 2.5×10^4, rpm = 800, $\bar{R} = 381$ mm, $\varepsilon = 30$, and $L/D_H = 12$. It is seen that the two observations made in the preceding paragraph for our study are also found for the study of Han et al. [13]. The quantitative difference in the level of $\overline{Nu}/Nu_0$ between the two works could be due to the difference in boundary conditions.

Figure 14 shows the ratio of the local Nusselt number with rotation to without rotation (Nu/Nu_S) vs streamwise location for $Re = 5000$ and $Ro = 0.13$, 0.22, 0.33 and 0.44. Dividing the local Nusselt number of the rotational

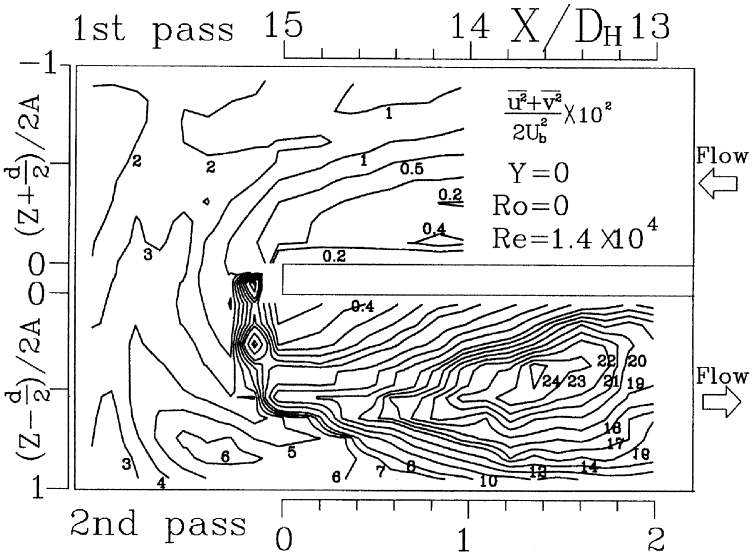

Fig. 10. Turbulent kinetic energy distribution near the 180° turn.

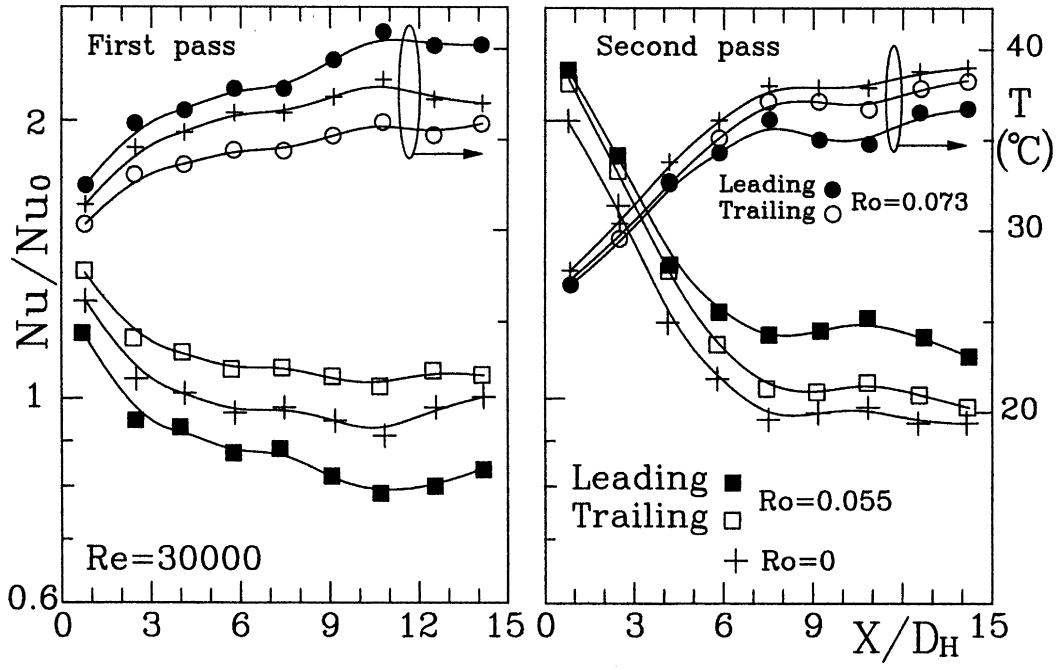

Fig. 11. Streamwise variation of wall temperature and local Nusselt number ratio for duct with and without rotation.

case by that of the measured stationary case of the same geometry rather than that of the heat transfer correlation (Dittus–Boelter, 1930) for the stationary circular tubes, the geometry effect of the 180° sharp turn on the heat transfer characteristics is reduced and the rotation effect could thus be more clearly revealed. Figure 14 depicts that, due to duct rotation, the difference in Nu/Nu_S between the leading and trailing walls is quite large at all locations of the first pass, especially in the middle part of the passage. In contrast, in the second pass the difference

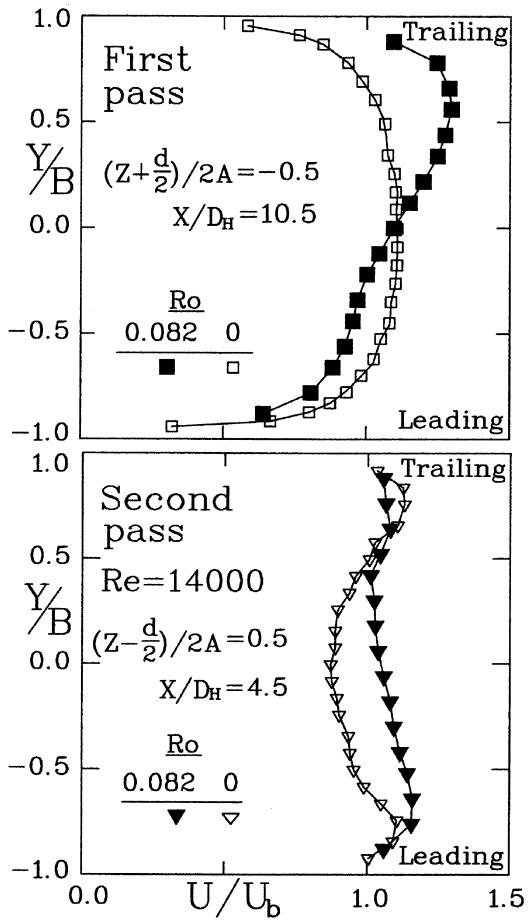

Fig. 12. Comparison of LDV measured streamwise velocity profiles between $Ro = 0$ and $Ro = 0.08$ for the first and second passages.

in Nu/Nu_S between the leading and trailing wall is relatively small, except for the rear part of the passage. The reason is that the heat transfer in the first part of the second pass is mainly dominated by the effect of turning geometry. Moreover, as a given X/D_H the scattering of Nu/Nu_s itself with Ro indicates the rotational effect on the local heat transfer characteristics. Figure 14 thus further shows that the rotation has a more prominent effect on the Nu/Nu_s around the first part of the first pass leading wall and around the rear part of the first and second passes trailing wall.

Quantitatively, in the first pass the percentage Nu/Nu_S enhancement of the trailing wall is maximum for $Ro = 0.44$ and occurs at $X/D_H = 12.5$ with a peak value as high as 105%; the heat transfer deterioration on the leading wall of the first pass is also most severe for $Ro = 0.44$ and occurs at $X/D_H = 10.8$ with a percentage Nu/Nu_S as low as 58%. The rotation effect is smaller in the second pass than in the first pass, similar to that found for a four-pass cooling channel [9–10]. In the second pass the greatest enhancement in Nu/Nu_S occurs at $X/D_H = 12.5$ on the leading wall for $Ro = 0.44$ and is 60%, and the lowest Nu/Nu_S occurs at $X/D_H = 2.5$ on the trailing wall for $Ro = 0.13$ and is 84%.

6. Conclusions

Based on the range of parameters examined and the results presented above, the main conclusions are

(1) For the stationary case, the complementary flow visualization and LDV measurements both indicate that the secondary flow induced by the turning curvature and turbulent enhancement, associated with flow separation by the sharp turning geometry, are the main reasons for the heat transfer enhancement in the first part of the second passage.
(2) For the stationary case, the secondary flow in the first part of the second pass is featured by two pairs of counterrotating vortex structures, one located inside and the other outside the separating bubble, which interact with each other and are more unstable than the single vortex pair prevailing inside the sharp turn. As a result, the turbulence intensity and in turn heat transfer are enhanced there.
(3) For the rotating case, the LDV measurements performed in the present study, lacking in the open literature, clearly demonstrate that the opposite directions of the Coriolis-induced secondary flow in the first and second pass are responsible for the skewness of the streamwise mean-velocity profile toward the trailing wall in the first pass and leading wall in the second pass, which in turn leads to the measured dominant local heat transfer enhancement on the trailing wall of the first pass and leading wall of the second pass.
(4) As the rotational number is increased, the length-averaged Nusselt number ratio ($\overline{Nu}/Nu_0$) is found to increase and decrease on the trailing and leading walls respectively, of the first pass, whereas $\overline{Nu}/Nu_0$ increases both on the trailing and leading walls of the second pass, although the increase rate is slower on the former.
(5) It is found that the rotation number has the largest effect on the difference in Nu/Nu_s between the leading and trailing walls in the middle part of the first pass and has the least effect in the first part of the second pass.

Acknowledgement

This research was partly supported by the National Science Council of the Republic of China under contract No. NSC-85-2212-E007-056

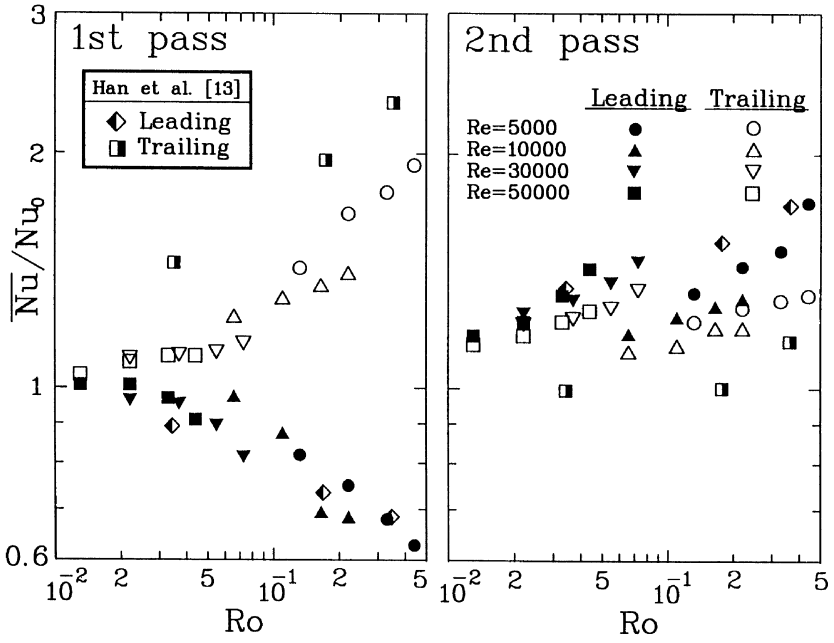

Fig. 13. Rotational effect on the averaged heat transfer coefficient ratios.

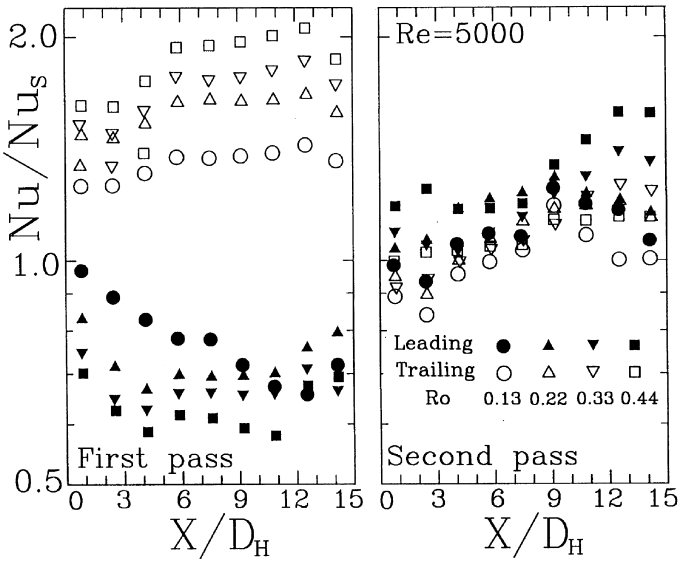

Fig. 14. Location effect on the heat transfer coefficient ratios for $Re = 5000$.

References

[1] Y. Mori, T. Fukada, W. Nakayama, Convective heat transfer in a rotating circular pipe (2nd report), International Journal of Heat and Mass Transfer 14 (1971) 1807–1824.

[2] R.J. Clifford, W.D. Morris, S.P. Harasgama, An experimental study of local and mean heat transfer in a triangular-sectioned duct rotating in the orthogonal mode, ASME Journal of Engineering for Gas Turbines and Power 106 (1984) 661–667.

[3] S.P. Harasgama, W.D. Morris, The influence of rotation on the heat transfer characteristics of circular, triangular, and square-sectioned coolant passages of gas turbine rotor blades, ASME Journal of Turbomachinery 110 (1988) 44–50.

[4] W.D. Morris, G. Ghavami-Nasr, Heat transfer measurements in rectangular channels with orthogonal mode rotation, ASME Journal of Turbomachinery 113 (1991) 339–345.

[5] C.Y. Soong, S.T. Lin, G.J. Hwang, An experimental study of convective heat transfer in radially rotating rectangular ducts, ASME Journal of Heat Transfer 113 (1991)604–611.

[6] W.D. Morris. R. Salemi, An attempt to uncouple the effect of Coriolis and buoyancy forces experimentally on heat transfer in smooth circular tubes that rotate in the orthogonal mode, ASME Journal of Turbomachinery 114 (1992) 858–864.

[7] C.R. Kuo, G.J. Hwang, Aspect ratio effect on convective heat transfer of radially outward flow in rotating rectangular ducts, International Journal of Rotating Machinery 1(1) (1994) 1–18.

[8] J. Guidez, Study of the convective heat transfer in a rotating coolant channel, ASME Journal of Turbomachinery 111 (1989) 43–50.

[9] J.H. Wagner, B.V. Johnson, T.J. Hajek, Heat transfer in rotating passages with smooth walls and radial outward flow, ASME Journal of Turbomachinery 113 (1991) 42–51.

[10] J.H. Wagner, B.V. Johnson, F.C. Kopper, Heat transfer in rotating serpentine passages with smooth walls, ASME Journal of Turbomachinery 113 (1991) 321–330.

[11] W.J. Yang, N. Zhang, J. Chiou, Local heat transfer in a rotating serpentine flow passage, ASME Journal of Heat Transfer 114 (1992) 354–361.

[12] J.C. Han, Y.M. Zhang, Effect of uneven wall temperature on local heat transfer in a rotating square channel with smooth walls and radial outward flow, ASME Journal of Heat Transfer 114 (1992) 850–858.

[13] J.C. Han, Y.M. Zhang, K. Kalkuehler, Uneven wall temperature effect on local heat transfer in a rotating two-pass square channel smooth walls, ASME Journal of Heat Transfer 115 (1993) 912–920.

[14] T.M. Liou, C.P. Yang, H.L. Lee, LDV measurements of spatially periodic flows over a detached solid-rib array, ASME Journal of Fluids Engineering 119 (1997) 383–389.

[15] S.J. Kline, F.A. McClintock, Describing uncertainties in single-sample experiment, Mechanical Engineering (January) (1953) 3–8.

[16] T.M. Liou, C.C. Liao, Flows in a curved combustor inlet with and without a guide vane, Journal of Propulsion Power 11 (3) (1995) 464–472.

[17] L.M.K. Boelter, G. Young, H.W. Iverson, An investigation of aircraft heaters—distribution of heat transfer rate in the entrance section of a circular tube, NACA TN 1451 Washington DC. 1948.

[18] S.V. Ekkad, J.C. Han, Local heat transfer distributions near a sharp 180° turn of a two-pass smooth square channel using a transient liquid crystal image technique, Journal of Flow Visualization and Image Processing 2 (1995) 285–297.